

CFD simulations of the flow around a cyclist subjected to crosswinds

Fintelman, Danielle; Hemida, Hassan; Sterling, Mark; Li, Francois-Xavier

DOI:

[10.1016/j.jweia.2015.05.009](https://doi.org/10.1016/j.jweia.2015.05.009)

License:

Creative Commons: Attribution-NonCommercial-NoDerivs (CC BY-NC-ND)

Document Version

Peer reviewed version

Citation for published version (Harvard):

Fintelman, D, Hemida, H, Sterling, M & Li, F-X 2015, 'CFD simulations of the flow around a cyclist subjected to crosswinds', *Journal of Wind Engineering and Industrial Aerodynamics*, vol. 144, pp. 31-41.

<https://doi.org/10.1016/j.jweia.2015.05.009>

[Link to publication on Research at Birmingham portal](#)

Publisher Rights Statement:

After an embargo period this article is subject to the terms of a Creative Commons Attribution Non-Commercial No Derivatives license.

Checked September 2015

General rights

Unless a licence is specified above, all rights (including copyright and moral rights) in this document are retained by the authors and/or the copyright holders. The express permission of the copyright holder must be obtained for any use of this material other than for purposes permitted by law.

- Users may freely distribute the URL that is used to identify this publication.
- Users may download and/or print one copy of the publication from the University of Birmingham research portal for the purpose of private study or non-commercial research.
- User may use extracts from the document in line with the concept of 'fair dealing' under the Copyright, Designs and Patents Act 1988 (?)
- Users may not further distribute the material nor use it for the purposes of commercial gain.

Where a licence is displayed above, please note the terms and conditions of the licence govern your use of this document.

When citing, please reference the published version.

Take down policy

While the University of Birmingham exercises care and attention in making items available there are rare occasions when an item has been uploaded in error or has been deemed to be commercially or otherwise sensitive.

If you believe that this is the case for this document, please contact UBIRA@lists.bham.ac.uk providing details and we will remove access to the work immediately and investigate.

CFD simulations of the flow around a cyclist subjected to crosswinds

Fintelman, D.M.*¹⁾, Hemida, H.²⁾, Sterling, M.²⁾, Li, F.-X.¹⁾

1) School of Sport, Exercise and Rehabilitation Sciences, University of Birmingham, UK

2) School of Civil Engineering, University of Birmingham, UK

** Corresponding author. E-mail address: dmfl44@bham.ac.uk. (D.M. Fintelman)*

Word count: 6656

ABSTRACT

For the first time, an extensive numerical study of the effect of crosswinds on the flow around a cyclist on a bicycle with stationary wheels has been undertaken for crosswind (yaw) angles ranging from 0° - 90°. The flow field and the aerodynamic forces have been obtained using three numerical techniques: Reynolds Averaged Navier Stokes (RANS), Detached Eddy Simulation (DES) and Large Eddy Simulation (LES). RANS models have been undertaken for all the range of yaw angles to provide a general insight of the flow around a cyclist, whilst DES and LES have been undertaken at 15° yaw angle in order to investigate the time-varying flow physics in detail. The aerodynamic forces have been compared with a series of wind tunnel experiments. The RANS results showed the development of large flow separation around the bicycle with increasing yaw angles. The instantaneous flow structures and the auto spectral densities of the time histories of the force coefficients are identified and revealed that the DES and LES turbulence models are able to predict the dominant frequencies found in the physical experiments. This work provides an improved understanding of the flow characteristics around a cyclist in crosswinds that will hopefully help to improve the safety of cyclists.

KEYWORDS

Crosswinds, cyclist, aerodynamics, turbulence model

HIGHLIGHTS

- The flow around a cyclist on a bicycle at different crosswinds is investigated
- The CFD results are compared with experimental data
- Different turbulence models are compared
- Flow structures around a cyclist in crosswinds are explored

1 INTRODUCTION

Crosswinds can have an impact on the performance, stability and safety of cyclists, e.g., ~5% of all single bicycle accidents are caused by crosswinds (Schepers and Wolt, 2012). Despite several fatalities, relatively little work has been undertaken investigating the effect of crosswinds with most numerical research focusing on minimising the overall aerodynamic drag (Defraeye et al., 2010a; Griffith et al., 2012; Hanna, 2002; Lukes et al., 2004). Two numerical cycling crosswind studies investigated the aerodynamics of isolated spoked bicycle wheels (Godo et al., 2009; Karabelas and Markatos, 2012). These studies enabled both the aerodynamic loads and flow structures around isolated bicycle wheels to be quantified. Both studies have demonstrated that the side forces acting on a spoked wheel are up to about 5-6 times higher than the drag forces, hence having an impact on the stability of the cyclist. However, a study by Barry et al. (2012), showed that the wheels and cyclist cannot be considered separately, due chiefly the flow interaction between them. In a numerical study reported by Hanna (2002), the full cyclist and bicycle system has been analysed. In the study a comparison has been made between disk and spoked rear wheels at different crosswind flow velocities (0-13 m/s). The side wind was positioned at a yaw angle of 90° to the cycling direction (the yaw angle is defined as the angle between the effective side wind, U_{eff} , and the direction of travel of the cyclist, U_x , as shown in Fig. 1). The study showed that a disk

wheel reduced the drag by approximately 2% compared to spoked wheels, but in a crosswind of ~9 m/s the side forces were doubled. As the research has been conducted for the British Cycling team, details of the simulations and the results are limited and without validation precaution has to be taken about the validity of the results.

Barry et al. (2012) undertook a series of wind tunnel experiments to investigate the effect of crosswind on the bicycle system for yaw angles up to 30° and discovered that when positioned in a time trial position, the side forces increase linearly with increasing yaw angles between 5-30°. It is found that the side forces are approximately double the drag forces at 15° yaw angle. It was also demonstrated that the wheel type, including spoked and disk wheels, has a significant effect on the aerodynamic drag and yaw moments. Although the work of Barry et al. study (2012) outlines the importance of examining crosswind at yaw angles often experienced by cyclists, it does not give real insight into the overall flow field. For many types of ground vehicles, the critical wind angle has been shown to be around 30°, such as busses (François et al., 2009; Hemida and Krajnović, 2009b), passenger cars (Ryan and Dominy, 1998) and trains (Diedrichs, 2010; Hemida and Krajnović, 2009a). For cyclists however, experimental results showed that there is no specific critical yaw angle (Fintelman et al. 2014). It is likely that even at small crosswind yaw angles (~15°), the stability and performance of the cyclist will be influenced by crosswinds. It is however reasonable to assume that with increasing yaw angles, it becomes more difficult for cyclists to control the bicycle. Several bicycle accidents are reported as a result of strong crosswinds ("Bike Rider Blown Over By Heavy Wind," 2011; "Bobridge blown off his bike," 2012; "Cyclist's death was an accident," 2001). The effect of crosswinds with yaw angles up to 90° has been investigated experimentally by Fintelman et al. (2014). The results showed that the actual aerodynamic loads arising from crosswinds can be up to about 2.5 times the aerodynamic drag with spoked wheels and cyclist in dropped position. In addition, it has been observed that the torso angle of the cyclist has little effect on the side force coefficient. In contrast, the bicycle significantly affects the aerodynamic forces; at large yaw angles, the bicycle is responsible for approximately 60% of the total side force coefficient. However, this study does not provide information about the flow

characteristics around the cyclist that causes the aerodynamic forces and moments. Noting this, the research discussed below was undertaken in order to provide detailed information on the overall aerodynamic forces and moments and to provide an insight into the surrounding flow field, thus laying the foundations for future improvements in cycling stability and performance.

In order to obtain accurate flow field and surface pressure of the bicycle and the cyclist, numerical simulations based on Reynolds Averaged Navier Stokes equations (RANS) using both $k-\epsilon$ and SST $k-\omega$ models have been undertaken. Yaw angles considered range between $0-90^\circ$. The surface pressure and the surface shear stresses are integrated to obtain the aerodynamic forces and moments on both the bicycle and cyclist with the results compared to previous physical simulations (Fintelman et al., 2014). In addition, Detached Eddy Simulations (DES) and Large Eddy Simulations (LES) are undertaken on a bicycle and a cyclist in order to gain an insight in the instantaneous flow physics around the cyclist at 15° yaw angle, since this is found to be a common crosswind yaw angle (Guzik et al., 2013) in cycling.

Section 2 of this paper briefly outlines the wind tunnel experiments that were undertaken in order to compare the numerical simulations, whilst section 3 outlines details relating to the computational models. Section 4 addresses the numerical details of the simulations, whilst section 5 outlines the numerical accuracy. This is followed by the results and discussion in section 6 and finally in section 7 the main conclusions are drawn.

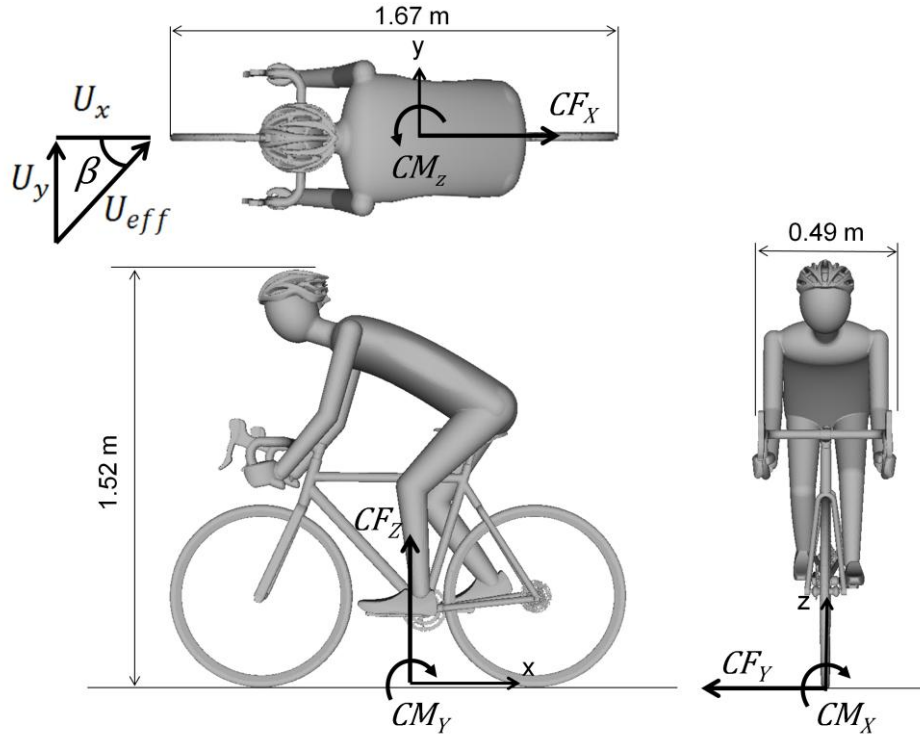


Fig. 1: Geometry and dimensions of cyclist and directions of the aerodynamic force and moment coefficients.

2 WINDTUNNEL EXPERIMENTS

Details relating to the physical simulations can be found in Fintelman et al. (2014) and are briefly reiterated for the benefit of the reader. The wind-induced forces on a bicycle with mannequin are measured in the open wind-tunnel facility at the University of Birmingham UK. The wind-tunnel has a cross-sectional area of $2 \times 2 \text{ m}^2$ and length of 10 m. A constant crosswind flow velocity, U_{eff} , of 9.91 m/s is maintained in the wind tunnel with a corresponding average turbulence intensity of 0.67 %. The mannequin is placed in a dropped position on a road bicycle with stationary wheels as shown in Fig. 2a and is connected to a six-component force balance (Kistler type 9281B, Kistler Instruments, Winterthur, Switzerland) which is used to measure the aerodynamic forces and moments. The aerodynamic forces were repeatable to within $\pm 0.05 \text{ N}$ and the uncertainty was approximately 2%.



Fig. 2: (a) Full-scale bicycle and mannequin used in wind tunnel experiments and (b) geometry of the bicycle and cyclist in simulations.

3 COMPUTATIONAL MODELS

To simulate realistic flow conditions, a high level of complexity and detail are maintained in the CAD model of the bicycle and mannequin (Fig. 2b). However, modelling of small objects such as the spokes and cables have been omitted to simplify the geometry. A generalized computational domain is used as shown in Fig. 3a, in which H (1.52m) represents the height of the cyclist from the ground. The dimensions of the computational domain are large enough that blockage area effects can be neglected (maximal blockage area of 0.3%). Similar to the wind tunnel setup, a uniform effective velocity, U_{eff} , of 9.91 m/s is applied for all different yaw angles, β . This gives a Reynolds number of 1.0×10^6 , based on the effective wind velocity and the height of the cyclist from the ground. The velocity in the main inlet direction, U_x , and in the crosswind inlet direction, U_y , is calculated as:

$$U_x = U_{eff} \cos(\beta), U_y = U_{eff} \sin(\beta). \quad (1)$$

No-slip boundary conditions are used on the surface of the model and on the ground to accurately match the wind tunnel experiments. A free-slip velocity boundary condition is applied on the upper boundary of the computational domain. In all simulations the wheels are considered static,

as the effect of the rotation on the wheels without spokes is found to be small; k- ϵ RANS simulations were undertaken without crosswinds and with crosswinds of 90° , in which the rims and tires rotated at 29.494 rad/s (equivalent to a tangential velocity of 9.91 m/s). The results (not reported here) showed that the aerodynamic coefficients in the main wind direction decreased by less than 1.8 % when implementing rotating rims and tires, which is within the limits of the uncertainties of the physical experiments. It is worth noting that rotation of the spokes can have an impact on the side force magnitude (Karebelas and Markatos 2012). However for ease of simplicity, spoke and leg movement was not included in the simulations.

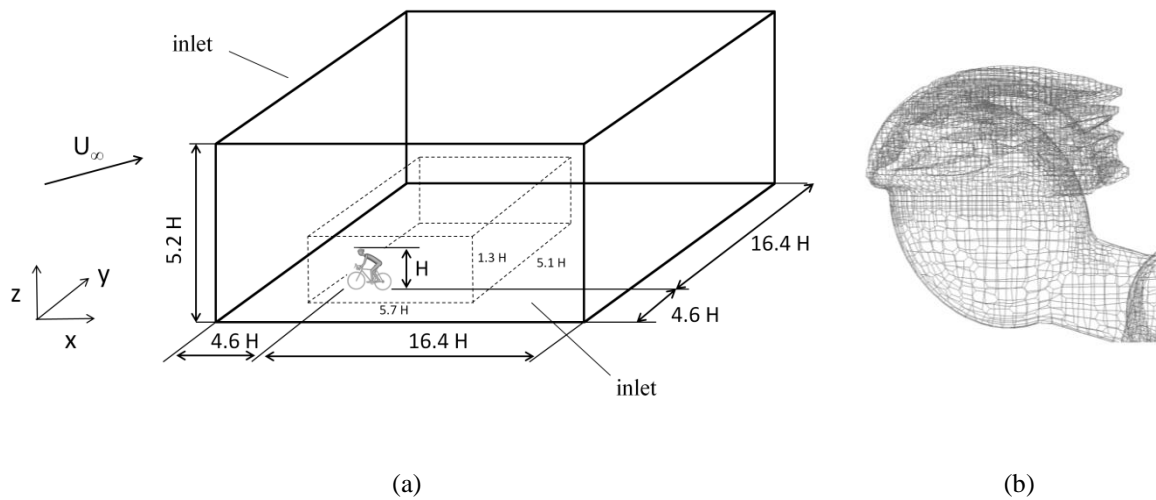


Fig. 3: (a) Computational domain, (b) surface mesh of the helmet of the cyclist for the RANS simulations.

RANS simulations were used to predict the average flow velocity, pressure and aerodynamic responses. Two different steady RANS simulations were performed with different turbulence models: the standard k- ϵ and the SST k- ω models. Wall functions are applied close to the wall based on the log-law. These turbulence models are commonly applied in numerical sport simulations, for example in swimming (Silva et al., 2008; Zaïdi et al., 2008), rowing (Zhang et al., 2009), ski jumping (Meile et al., 2006) and bobsleigh (Dabnichki and Avital, 2006). They have

also been shown to give a reasonable performance when applied in cycling (Defraeye et al., 2010b; Griffith et al., 2014).

In addition to the simulations using RANS models, the more computationally expensive but accurate standard detached eddy simulation (DES) are undertaken for the flow at 15° yaw angle. This is to provide information about the instantaneous and time-averaged flow at this particular yaw angle. The hybrid DES approach combines the RANS close to the walls and Large-eddy simulation (LES) in the region outside the boundary layers. This model replaces the turbulent length scale function l_{RANS} with a modified length scale function, l_{DES} :

$$l_{DES} = \min(l_{RANS}, C_{DES}\Delta) \quad (2)$$

where C_{DES} is a constant (0.65) and Δ is the largest dimension of the grid cell in all three directions, i.e., $\Delta = \max(\delta x, \delta y, \delta z)$. The length scales increases with the distance from the wall. Therefore, close to the wall the model behaves like the RANS model and the length scale is:

$$l_{DES} = l_{RANS} \ll C_{DES}\Delta. \quad (3)$$

In the far field the length scale is given by:

$$l_{DES} = C_{DES}\Delta \ll l_{RANS} \quad (4)$$

The most commonly used Spalart-Allmaras one-equation turbulent model is applied (Spalart and Allmaras, 1994). DES has been successfully used for the aerodynamics of a ground vehicle (Flynn et al., 2014; Hemida and Krajnović, 2009b).

Finally, the Large Eddy Simulations (LES) are used to make an accurate comparison of the simulation results of the different turbulence model approaches at a common crosswind yaw angle of 15°. LES is the most computational expensive turbulent model used in this research, but is considered to be the most accurate of all mentioned models, particularly when large scale flow unsteadiness is significant (which is likely to be the case for cyclists and bicycles). With the increase in computational power, LES has been used extensively in the study of the flow around small scale models of trains and cars subjected to cross winds (Hemida and Baker, 2010; Hemida

and Krajnovic, 2010; Tsubokura et al., 2010). In the LES approach, the large eddies containing the most energy are resolved, whilst a sub-grid scale model is used for the eddies smaller than the grid size. The velocity is decomposed into a filtered part and sub-grid scale component. The filtered Navier-Stokes equations are derived for the large scale eddies. The filtered continuity and momentum equations for an incompressible flow are:

$$\frac{\partial \bar{u}_i}{\partial t} + \frac{\partial \bar{u}_i \bar{u}_j}{\partial x_j} = -\frac{1}{\rho} \frac{\partial \bar{p}}{\partial x_i} + 2 \frac{\partial}{\partial x_j} (v + v_t) (\bar{S}_{ij} - \partial \tau_{ij}^r), \quad (5)$$

$$\text{and} \quad \frac{\partial \bar{u}_i}{\partial x_i} = 0,$$

where \bar{u}_i and \bar{p} are the filtered velocity and pressure, v_t the turbulent viscosity, \bar{S}_{ij} the resolved strain rate tensor and τ_{ij}^r the subrid scale stresses. The Smagorinsky sub-grid model is used to derive the sub-grid scale Reynolds stresses by calculating the turbulence viscosity:

$$v_t = (C_S f_d \Delta)^2 \sqrt{2 \bar{S}_{ij} \bar{S}_{ij}}, \quad (6)$$

where C_S the Smagorinsky constant (0.1) and f_d is the van Driest damping function.

4 NUMERICAL DETAILS

The open-source CFD package ‘‘OpenFOAM’’ is used to perform all the simulations with the three dimensional finite volume to solve the flow. The SIMPLE algorithm is implemented in the simulations to couple the pressure and velocity. In the RANS simulations, the gradients are computed with a least square second order scheme. The pressure interpolation is performed with the second order central differencing scheme. The convection and viscous terms are solved with the second order upwind scheme. In the DES and LES simulations, the time discretization has been approximated by the second order implicit backward scheme. Gradients are computed with the second order central differencing scheme. A central difference-upwind stabilised transport scheme is used for the convection terms. This scheme blends 25% second order upwind with 75%

central difference interpolation to stabilise the solution whilst maintaining second order behaviour. The induced numerical dissipation plays an important role in stabilizing the convergence. In the transient simulations, a constant time step of $\Delta t = 0.00001$ sec has been used. This time step ensures that the maximum Courant-Friederichs-Lewy (CFL) number is lower than 1.0. The time history of the aerodynamic coefficients has been obtained for each time step. Convergence is monitored and simulations stopped when the residuals were stable and the maximum normalized residual of each turbulent equation has been converged to at least 10^{-4} . The total wall time of the fine mesh of the RANS, DES and LES approach running at 16 processors was about 17 hours, 905 hours and 1357 hours respectively.

5 NUMERICAL ACCURACY

To investigate the effect of the grid size on the RANS results, three different meshes (coarse, medium and fine) are evaluated with different number of nodes: 3.5×10^6 , 8.7×10^6 and 17.9×10^6 , respectively. The averaged normal wall distance y^+ of the cyclist for the different RANS meshes are 82, 60 and 43 respectively. Fig. 3b shows an example of the surface mesh of the cyclist's helmet. Fig. 4 shows the surface pressure of the cyclist at a height of $0.7 H$, obtained from the RANS coarse, medium and fine meshes. The pressure distribution is expressed in terms of the local pressure coefficient, C_p , which is defined as:

$$C_p = \frac{p - p_\infty}{0.5 \rho U_{eff}^2}, \quad (7)$$

where p is the local pressure, p_∞ the free stream pressure and ρ the air density. A good agreement (Root Mean Square error = 0.09) is found between the RANS fine and medium mesh.

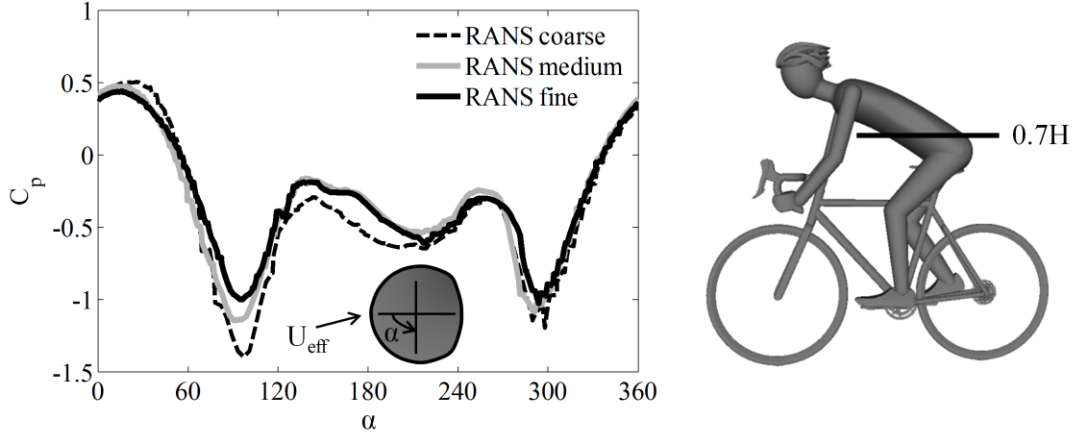


Fig. 4: Pressure distribution around the surface of the main body of the cyclist obtained from the coarse, medium and fine mesh of the RANS $k-\epsilon$ simulations at $\beta=15^\circ$.

In addition to the pressure distribution, the aerodynamic forces (expressed in coefficient form) were compared. The drag force coefficient CF_X , side force coefficient CF_Y , lift force coefficient and CF_Z are defined as:

$$CF_X = \frac{F_X}{0.5A\rho U_{eff}^2}, CF_Y = \frac{F_Y}{0.5A\rho U_{eff}^2}, CF_Z = \frac{F_Z}{0.5A\rho U_{eff}^2}, \quad (8)$$

where A is the total frontal area of the cyclist and bicycle at 0° yaw angle (0.55 m^2), U_{eff} is the effective flow velocity (m/s), and F_X , F_Y , and F_Z are the drag force, side force and lift force, respectively. The coordinate system adopted and thus the directions of these forces are shown in Fig. 1. The aerodynamic force coefficient for the different grid sizes of the RANS models are shown in Table 1. The results of the RANS medium simulation compare well to those of the fine simulation. The grid convergence index (GCI) is used to quantify the error of the fine grid (Celik et al., 2008) and is defined as:

$$GCI_{fine} = \frac{F_S |\epsilon|}{r^p - 1}$$

where F_S is the safety factor, ϵ the relative error between the fine and medium mesh, r the grid refinement factor and p the order of accuracy. The safety factor is set to 1.25. The numerical uncertainty in the fine grid solution for the drag coefficient CF_X and the side force coefficient CF_Y

are 0.4 % and 0.2 % respectively. These levels of agreement between the results obtained from the RANS fine and medium meshes suggest that the resolution of the fine mesh is adequate to correctly predict the flow and hence no further mesh refinement is needed. From this point all the RANS results are from the fine mesh unless otherwise explicitly stated.

In the RANS simulations, standard wall functions are used to solve the near wall region, requiring a less refined mesh close to wall. In the LES simulations, the accuracy of the results is dependent on the grid size. In particular in the near wall region a fine mesh is required. Therefore, an additional refinement box of dimensions 3.2 m x 0.8 m x 1.66 m (L x W x H) is added into the LES mesh. In addition, a higher surface based refinement level is applied. The total number of nodes in the LES mesh is 26.7×10^6 , consisting of 84% of hexahedra elements, 15% polyhedral elements and 1% of prisms, tetrahedral wedges and tetrahedral elements. To be able to make an objective comparison between the LES and the DES simulation results, an identical mesh is used in both simulations. This allows a direct comparison of these two turbulence approaches, the grid influence being eliminated. This implies that the transition from LES to RANS in the DES will take place closer to the wall and consequently the DES will acts more like a LES model in most of the computational domain. A mesh sensitivity analysis has been carried out on the DES and LES simulation by performing a simulation on an even finer mesh, consisting of 41.7×10^6 nodes. The normal wall distances of the cyclist for the coarse and fine mesh are about 5.2 and 3.4 respectively. The results illustrate a reasonable agreement with the results of the coarser DES and LES mesh as shown in Table 1 (CF_x error difference of about 1.0% and 0.3% respectively).

Table 1: Force coefficients refinement of the RANS $k-\varepsilon$ model and the DES simulations

| | CF_X | CF_Y | CF_Z |
|-------------|--------|--------|--------|
| RANS Coarse | 0.653 | 0.148 | 0.116 |
| RANS Medium | 0.586 | 0.227 | 0.081 |
| RANS Fine | 0.596 | 0.231 | 0.099 |
| DES Coarse | 0.508 | 0.243 | 0.182 |
| DES Fine | 0.513 | 0.250 | 0.180 |
| LES Coarse | 0.612 | 0.211 | 0.184 |
| LES Fine | 0.610 | 0.232 | 0.160 |

6 RESULTS AND DISCUSSION

6.1 Aerodynamic force coefficients

Fig. 5a shows the variation of the aerodynamic drag forces, side forces, lift forces and rolling moments of the bicycle and cyclist for different yaw angles, obtained from the RANS simulations and the experiments. The rolling moment coefficient CM_X is defined as:

$$CM_X = \frac{M_X}{0.5AH\rho U_{eff}^2}, \quad (9)$$

where M_X is the rolling moment. The direction of application of the rolling moment is shown in Fig. 1. The rolling moment tends to rotate the bicycle about its longitudinal axis. For stability and safety, the side force and rolling moment coefficients are most important. The results show that the aerodynamic side force and the drag coefficients are a function of yaw angle and for the case of CF_Y , significant variations can be observed. Large side forces, yaw moments and roll moments are likely to have a strong impact on the bicycle stability. The RANS simulations illustrate similar trends to the experimental data with small variations in the drag force ($\sim 9\%$) and lift force ($\sim 7\%$) across the entire range of the examined yaw angles (Fig. 5a). Larger variations are observed for

the side forces (~21%) and the rolling moment (~11%). Of the two RANS model approaches, the k- ϵ model demonstrates the best performance, showing a better prediction of the drag and side force coefficients. The better performance of the k- ϵ model is likely caused by the over prediction of the turbulent kinetic energy and hence the turbulent viscosity, which has an impact on the aerodynamic forces (Makowski and Kim, 2000). The overall under prediction of the aerodynamic forces of the k- ϵ and SST k- ω models are likely to be a consequence of the failure of the RANS models to correctly represent the flow physics in areas of considerable separation and reattachment regions. Furthermore, it is possible that for large yaw angles ($> 60^\circ$), ~52% of the under prediction of the side forces may be due the treatment of the modelling of the wheels (Karabelas and Markatos, 2012). However, it should be noted that this explanation should be interpreted with care since Karabelas and Markatos (2012) did not consider the interaction between bicycle and cyclist and this is felt to have a larger influence on the aerodynamics forces.

The results of the DES and LES are in a reasonable agreement with the experimental data as shown in Table 2 and Fig. 5b. It should be noted that at 15° yaw angle the actual magnitude of the side forces are small, which ensures that even small differences between the actual and predicted results in a relatively large percentage error. With increasing yaw angles, the percentage differences will reduce. All the CFD techniques under predict the drag and side force coefficients at the crosswind yaw angle of 15° . The under prediction could be assigned to a range of different small factors, which together add up to quantifiable differences. First of all there are small geometrical differences and simplification of the geometry, such as the exclusion cables and spokes. The contribution of the spokes to the total side forces at different yaw angles is numerically investigated by Karabelas and Markatos (2012). They found that for an isolated stationary wheel at a yaw angle of 15° , the spokes increase the side forces by about 0.5N. The spokes could therefore explain approximately 60% of the under prediction of the side forces.

Secondly, it should be appreciated that in the physical modelling, there was slight buffeting of the mannequin in the y-direction largely due to the mannequin induced turbulence, which given the nature of the experiments meant that the geometry of the mannequin-cycle altered slightly during

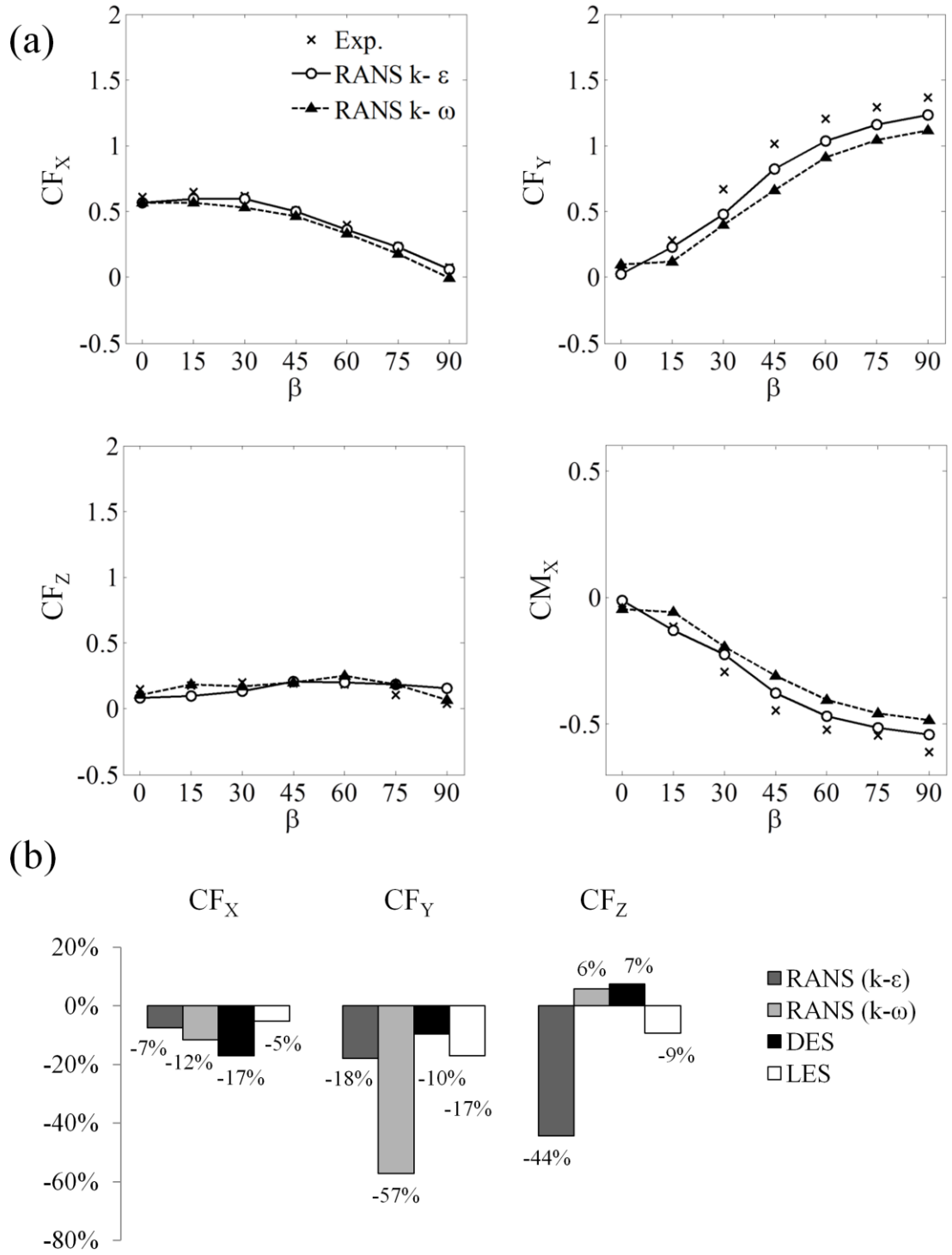


Fig. 5: Comparisons of the aerodynamic force coefficients obtained in the experiments and different turbulence models expressed as: (a) absolute value at different yaw angles, (b) percentage error for the drag at 15° crosswind yaw angle.

the tests compared to the numerical simulations. Finally, the variations could be associated with the inaccuracy of the turbulence models to capture all scales and to correctly predict the flow separation and attachments. The best performance is seen for the LES simulations, having a drag coefficient error of approximately 5% compared with the experimental data (Fig. 5b). The DES approach shows a reasonable good agreement for the lift and side forces (variation <10%), however larger discrepancies of about 17% are found for the drag force, which is the dominating force direction at the 15° crosswind yaw angle. The less accurate performance of the DES compared with the LES is a result of the capturing of less eddies and the not resolving of the eddies scaled with the grid cells in the boundary layer.

The relative contributions of the mannequin and bicycle to the aerodynamic coefficients are shown in Table 2. Comparable results are found for the simulations and the experiments. About 70% of the total drag force coefficients CF_x and rolling moment coefficients CM_x are caused by the mannequin in both the experimental work and simulations. The contribution is smaller for the side force coefficients CF_y , where the mannequin contributed to about ~34-49%. In the simulations, the bicycle has a lower contribution to the CF_y , which is likely caused by the simplification of the geometry (i.e. no spokes, cables, chain etc). Finally, for both the experiments and the simulations, the main contribution of the lift force coefficients is the mannequin (around 90-110%).

In the CFD results, a distinction is made between the pressure forces and the skin friction forces. The skin friction is caused by the viscous stress in the boundary layer around the bicycle and cyclist. In all the numerical investigations undertaken in this report, approximately 3% of the total drag forces and approximately 2% of the total side forces can be attributed to skin friction respectively. These relatively low viscous forces are comparable with similar investigations concerning an isolated cyclist (Defraeye et al., 2010b). As the mannequin-bicycle model used in the CFD calculations is smoother than that in the physical experiments, it is expected that the predicted viscous forces in the experiments are slightly higher than the computed ones. However, due to the nature of the physical experiments this hypothesis cannot be verified.

Table 2: Aerodynamic coefficients for the DES and LES simulations together with the experimental results at $\beta=15^\circ$. The total aerodynamic coefficients and the relative contribution of the bicycle and mannequin are given. The percentage of the relative contribution of the mannequin and bicycle to the total aerodynamic coefficients are presented.

| | | Total (Mannequin and Bicycle) | Mannequin | Bicycle |
|--------|-------------|-------------------------------|---------------|--------------|
| CF_x | DES | 0.513 | 0.359 (70%) | 0.154 (30%) |
| | LES | 0.610 | 0.440 (72%) | 0.171 (28%) |
| | Experiments | 0.644 | 0.449 (70%) | 0.195 (30%) |
| CF_y | DES | 0.250 | 0.123 (49%) | 0.128 (51%) |
| | LES | 0.232 | 0.107 (46%) | 0.125 (54%) |
| | Experiments | 0.281 | 0.095 (34%) | 0.186 (66%) |
| CF_z | DES | 0.180 | 0.197 (109%) | -0.015 (-8%) |
| | LES | 0.160 | 0.171(107%) | -0.011 (-7%) |
| | Experiments | 0.178 | 0.155 (87%) | 0.023 (13%) |
| CM_x | DES | -0.107 | -0.070 (65%) | -0.037 (35%) |
| | LES | -0.104 | -0.069 (66%) | -0.035 (34%) |
| | Experiments | -0.114 | -0.083 (73%) | -0.031 (27%) |

6.2 Time-averaged flow

Fig. 6 shows the surface pressure distribution, obtained from the k- ϵ simulation at different yaw angles. At $\beta = 0^\circ$, low pressure regions appear at the sides of the body where the vortex shedding takes place. By increasing the yaw angle, an area of suction pressure develops at the back of the cyclist and high pressure regions develop on the upper lower limbs and the abdomen. At 90° yaw angle, high pressure areas develop at the windward side of the cyclist, whilst the back and leeward sides of the cyclist are dominated by low pressure regions. At this yaw angle, the suction pressure

is balanced by a developed suction pressure on the front side of the cyclist (not shown in the Figure) and this explains the low drag coefficient at large yaw angles ($> 60^\circ$).

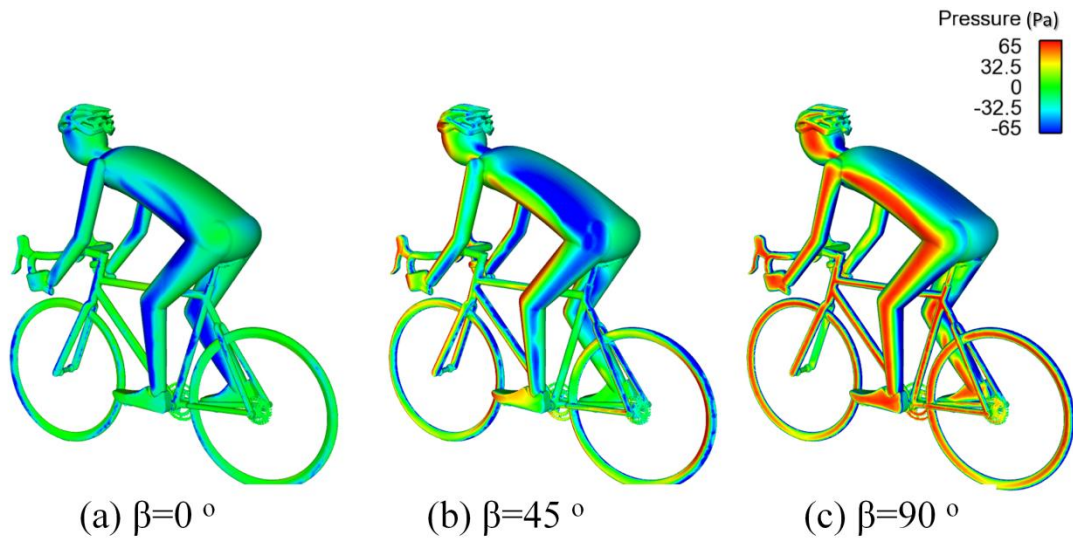


Fig. 6: Pressure distribution on the cyclist at different crosswind yaw angles obtained from the RANS $k-\epsilon$ simulations.

The isosurface of the pressure around the cyclist at $C_p = -0.240$ for yaw angles of 0° and 60° is shown in Fig. 7. For the case of no crosswind (0° yaw angle), the pressure is approximately symmetrical with the concentration of low pressure around the sides of the cyclist. However, at a yaw angle of 60° , the low pressure surface is located behind and at the leeward side of the cyclist and bicycle. In particular at large yaw angles, the bicycle starts to contribute to the turbulent flow around the cyclist which leads to an increase in the side force and rolling moment. This phenomenon has been also observed in the physical experiments, where for 60° yaw angle the bicycle was found to account for approximately 60% of the total side force coefficient; whilst at 0° yaw angle the bicycle accounts for only about 20% of the total drag (Fintelman et al., 2014).

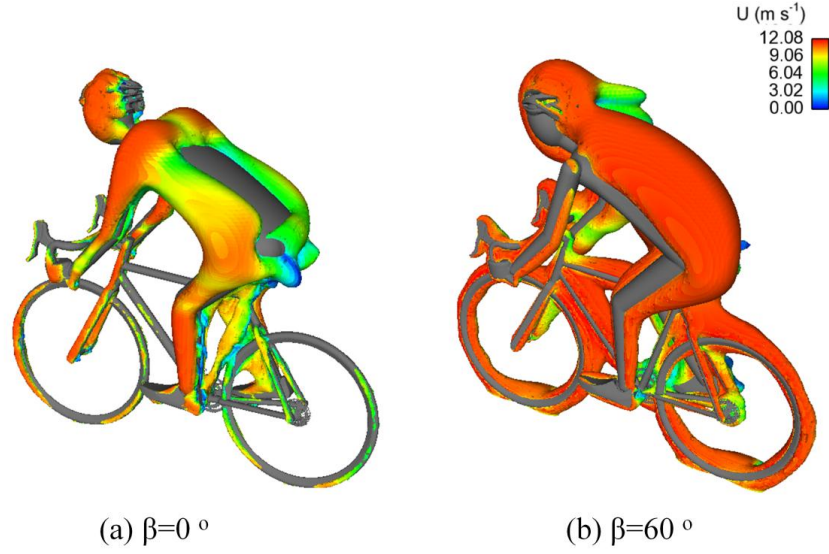


Fig. 7: Isosurface of the pressure at $C_p = -0.240$ at different yaw angles, coloured with the instantaneous velocity and obtained from the RANS $k-\epsilon$ simulations; (a) $\beta=0^\circ$; (b) $\beta=60^\circ$.

The time-averaged pressure at different locations in the direction of the main flow at a crosswind yaw angle of $\beta=15^\circ$ is shown in Fig. 8. The positions considered are at a distance of $0.3H$, $0.5H$, $0.7H$ and $0.9H$ from the cyclist. The negative peak pressure in the wake decreases with increasing distance from the cyclist. All turbulence models considered are approximately consistent with one another in terms of identifying the location of the peak pressure. The largest coefficient of pressure can be found at a height of about $0.6H$, caused by flow structures that are separated from the back of the cyclist. The deviations with respect to the LES simulation are largest for the RANS $k-\epsilon$ simulation. Smaller deviations are observed between the more accurate LES and DES results.

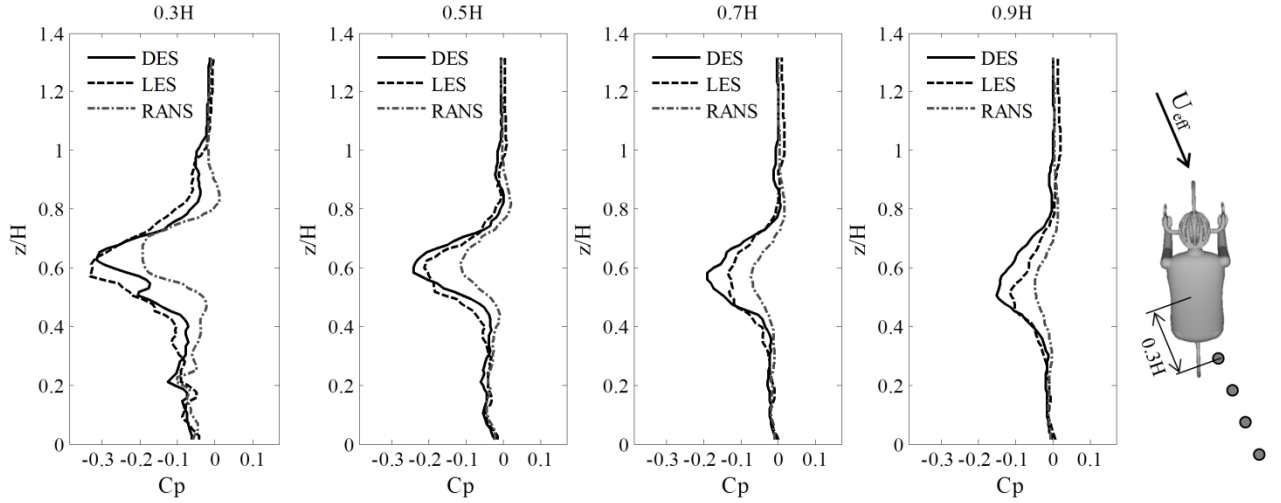


Fig. 8: Time-averaged vertical pressure lines at different locations in the wake of the cyclist at yaw angle $\beta=15^\circ$ at a distance of $0.3H$, $0.5H$, $0.7H$, $0.9H$ from the cyclist in the main flow direction.

6.3 Instantaneous flow

Although RANS simulations are computationally efficient due to their nature, obtaining instantaneous flow information by such methods is not possible. Therefore DES and LES are used to determine the instantaneous flow features. Fig. 9 shows the isosurface of the instantaneous pressure around the cyclist at $C_p = -0.240$ and a crosswind angle of 15° of the DES and LES simulations. As the centres of the flow vortices are normally associated with low pressure, these isosurface of constant pressure can be used to infer the flow structures around the bicycle and cyclist. The results of the DES (Fig. 9a) and LES (Fig. 9b) at random instantaneous time points look qualitatively similar. In both approaches the instantaneous flow structures show large vortices shed at the back and leeward side of the body into the wake flow. The flow separates at the back side of the helmet and the back of the cyclist to form large unsteady structures. Once these structures completely separate from the surface they tend to form vortex tubes with axis parallel to the flow direction as shown in Fig. 9.

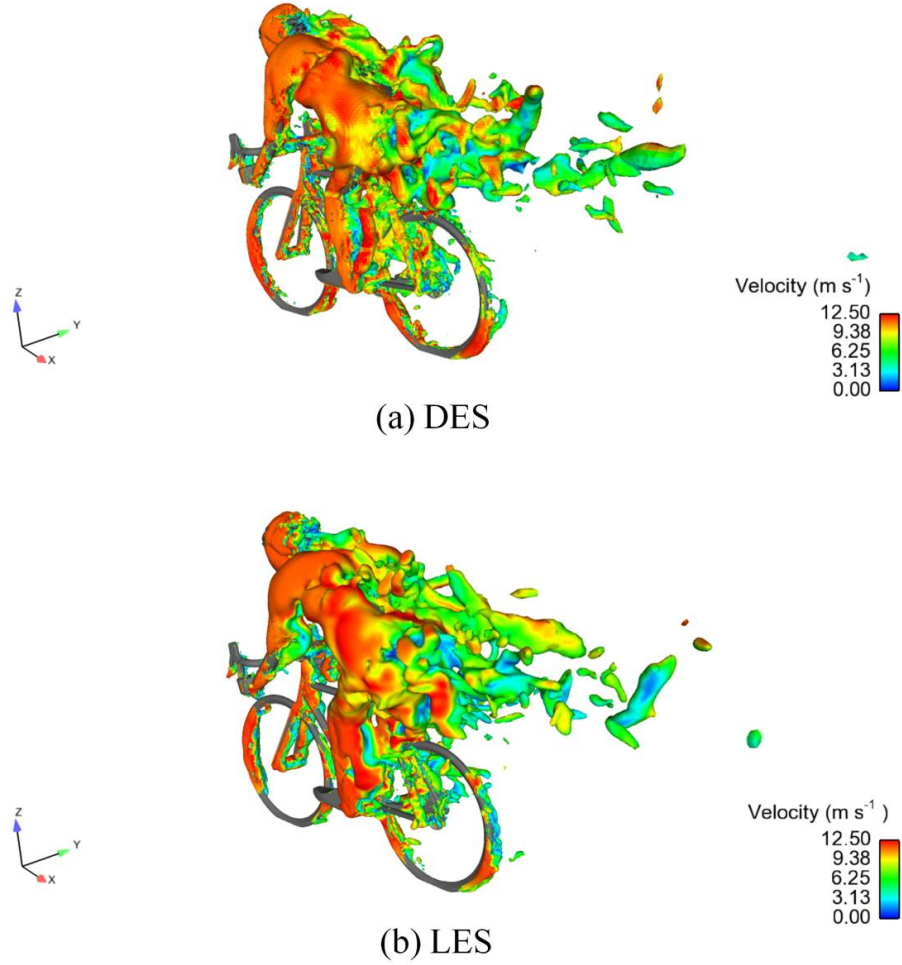


Fig. 9: Instantaneous flow structures around the cyclist subjected to crosswind with a yaw angle of 15° at $C_p = -0.240$ and coloured with the instantaneous velocity, obtained from the (a) DES approach and (b) LES approach.

The vortex cores of the flow around the cyclists are found by means of Eigen analysis. This method is based on an algorithm of Sujudi and Haimes (1995) and uses the Eigen value of the velocity gradient tensor to identify the vortex cores. The vortex cores help to give an insight into the possible distribution of the vortices around the cyclist. The locations of the instantaneous vortex cores in the flow around the bicycle at 15° yaw angle for the LES and DES turbulence models are shown in Fig. 10. These vortices are predominantly developing and stretching along the direction of the main flow and showing the largest strength closest to the body. This underpins the observation based on the pressure isosurface shown in Fig. 9. Similar main flow vortices are

obtained by LES and DES as shown in Fig. 10 in terms of the instantaneous vortex cores. These main vortices are rather small and can be described as follows:

- Vortex V1 appears due to separation of the flow around the helmet.
- Vortex V2 originates from a focus very close to the cyclists' gluteus maximus.
- Vortex V3 and V4 appear at the leeward side of the upper body and originate very close to the back side of the upper arm.

The LES resolves more of the small vortex structures than the DES approach and thus many small-scale structures are found predominantly around the lower back of the cyclist compared to the DES simulations.

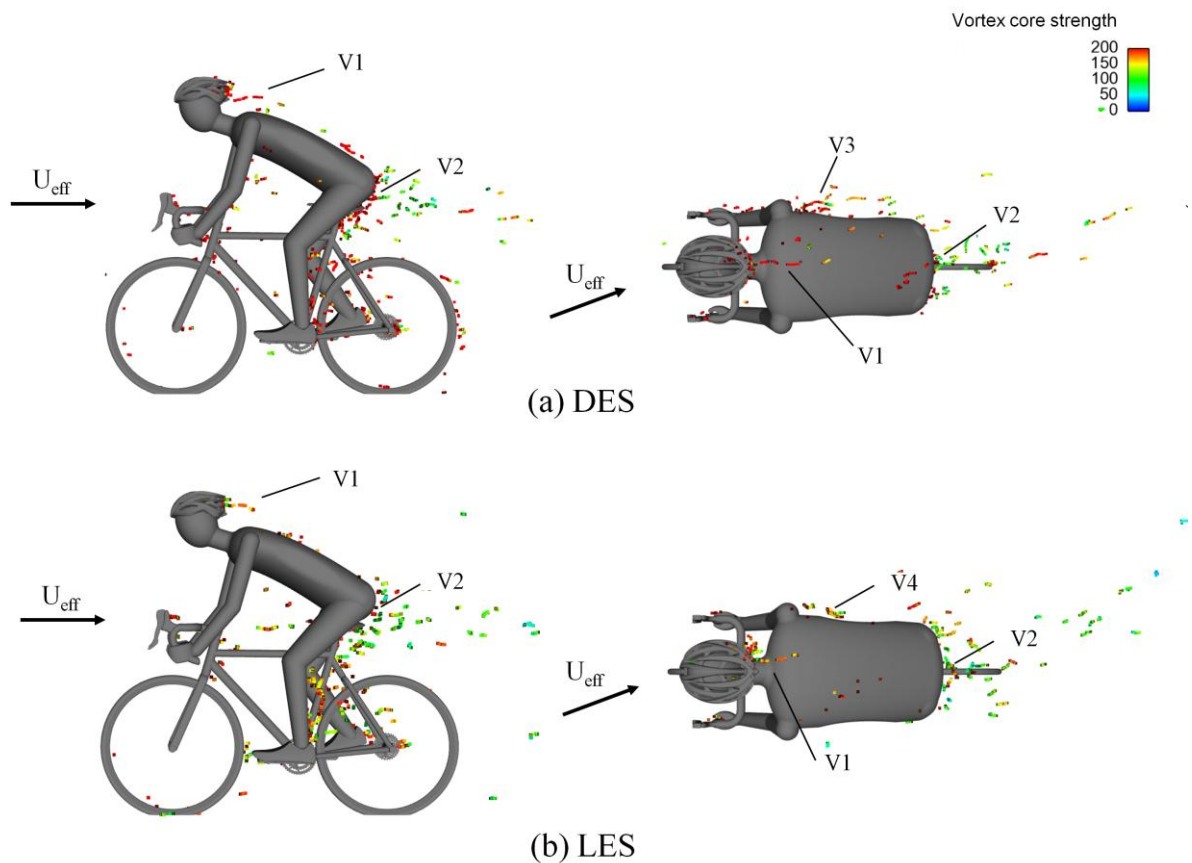


Fig. 10: Location of the instantaneous vortex cores in the flow around a cyclist shown from the side view and top view, obtained from the (a) DES simulation and (b) LES simulation. The vortex cores are coloured by the vortex core strength.

The aerodynamic coefficient time histories are used to reveal the effect of the turbulence on the forces and moments. It is assumed that the flow is statistically stationary. The time, t , is expressed in a form of dimensionless time, t^* , as:

$$t^* = \frac{t U_{eff}}{H}. \quad (10)$$

The time histories of the drag force, side force, lift force and rolling moment coefficients obtained by the DES and LES simulations are shown in Fig. 11. The shedding of vortices at the back and leeward side of the body into the wake flow shown in Fig. 9, contributes to relatively large observed variation in the time history of the aerodynamic force coefficients CF_X and CF_Y shown in Fig. 11. The largest variations in force coefficients are observed in the CF_Y , which is predominantly caused by the large vortices shed from the mannequin. As shown in Table 3, the standard deviations of the time histories of both turbulence model approaches are in the same order of magnitude. The standard deviations of the aerodynamic coefficients of the experiments are on average about 3 times larger than those of the simulations. These variations are likely not to be a result of the uncertainties of the force balance, but arise from vibrations and natural frequencies of the mannequin and bicycle system, causing stronger vortex shedding around the cyclist as shown in Fig. 9.

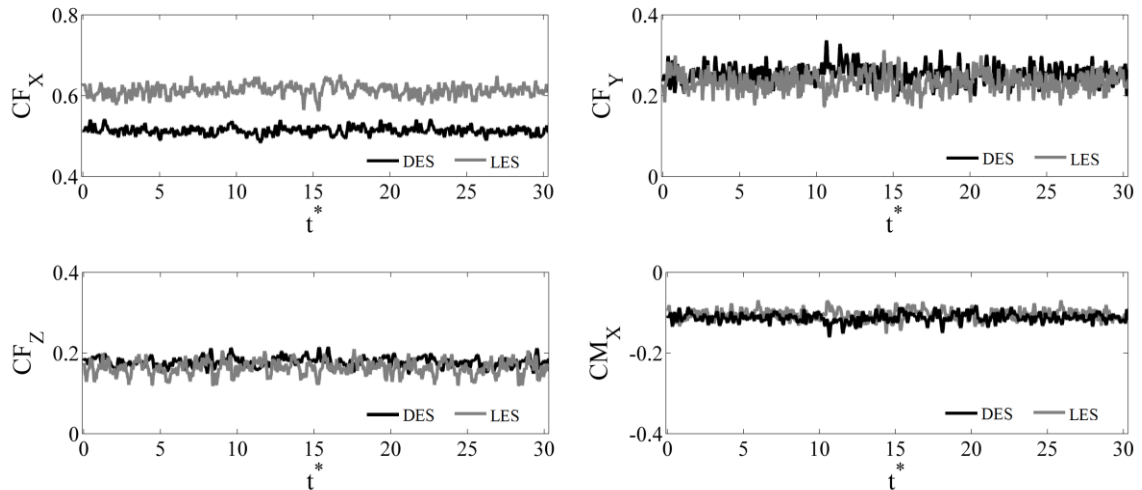


Fig. 11: Time history of the aerodynamic coefficients obtained from the fine mesh DES and LES simulations.

Table 3: Mean and standard deviation of the aerodynamic force responses of the DES simulations, LES simulations and windtunnel experiments at 15° crosswind yaw angle.

| | Mean DES | Mean LES | Mean Exp | Std DES | Std LES | Std Exp |
|-----------------|----------|----------|----------|---------|---------|---------|
| CF _x | 0.513 | 0.610 | 0.644 | 0.010 | 0.014 | 0.046 |
| CF _y | 0.250 | 0.232 | 0.281 | 0.022 | 0.023 | 0.075 |
| CF _z | 0.180 | 0.160 | 0.178 | 0.012 | 0.017 | 0.042 |
| CM _x | -0.107 | -0.104 | -0.114 | 0.011 | 0.013 | 0.016 |
| CM _y | 0.292 | 0.355 | 0.383 | 0.006 | 0.009 | 0.014 |
| CM _z | -0.017 | -0.018 | -0.008 | 0.004 | 0.004 | 0.010 |

A Fourier transform resulting in the power spectra of the time-varying force coefficients is used to resolve the dominating frequencies. The aerodynamic force frequencies provide an insight into the turbulent frequencies (f) in the flow and represent the crosswind induced force frequencies. The frequencies are expressed in Strouhal number:

$$St = \frac{fH}{U_{eff}} \quad (11)$$

The power spectra are normalized by the root means square of the turbulent frequencies. All high amplitude peaks in the auto spectral densities of the simulations (Fig. 12a and 12b) can be found in the range $St = 0 - 7$. For the DES simulations, the dominant peak in the drag force coefficient is found at $St = 0.49$, which corresponds to 3.2 Hz. The dominant peak in the LES simulations is at $St = 0.99$, corresponding to 6.5Hz. In the side force coefficients, multiple high amplitude peaks can be found. These peaks are caused by the large range of length scales due to variety of surfaces and angles of the cyclist and bicycle seen by the free stream flow. One of the main frequency components in the side force coefficient is at $St = 2.83$ (E5), corresponding with 18.5 Hz. This frequency coincides with the frequency of the integral length scale of the drag coefficient. The integral length scale describes the size of the large energy containing eddies in the flow. In the side force coefficient frequency spectrum these large eddies originate from the mannequin.

Another dominant side force frequency is found at around $St = 1.64$ (E4), which corresponds to 10.7 Hz. The lift force of the DES simulations has a characteristic frequency at $St = 0.20$, corresponding to 1.3 Hz. The dominant frequency of the LES simulation is at $St = 0.99$. This peak in the lift force coefficients spectrum is identical to the dominant peak found in the drag forces of the LES simulations.

The auto spectral densities of the simulations are compared with experimental data. Any structural contributions of the bicycle and mannequin have been filtered from the spectra. The experimental force coefficient time histories are shown in Fig. 12c and are dominated by low frequency contents ranging between $St = 0$ and $St = 9$. The values of the dominant frequencies in the experimental work (E1-E7) can be found in Table 4. All dominant frequencies in the auto spectral density of the experiments are also found in the frequency spectra of the DES and LES simulations, albeit not of the same magnitude. This indicates that both approaches are able to predict the important instantaneous flow features. In the drag force coefficient spectrum, which is the major wind direction, similar dominant frequencies (E1-E3) are found in the power spectrum of the LES. However, the highest absolute spectral power is observed in the side force coefficient direction. The dominant peaks E4 and E5 in the side force direction are similar to the dominant peaks of the LES and DES simulations. The normalized spectral power at these frequencies in the LES approach is higher than that of the DES simulations. This suggests that the LES simulations are better capable of predicting the reattachment and separation in the side force direction. Finally, the dominant lift force coefficient frequencies, E6 and E7, are found in the simulations. The relative large discrepancy of the behaviour of the lift force coefficient spectra between the experiments and the numerical results can be explained by the small magnitude of this force and the associated uncertainties which arise when normalising.

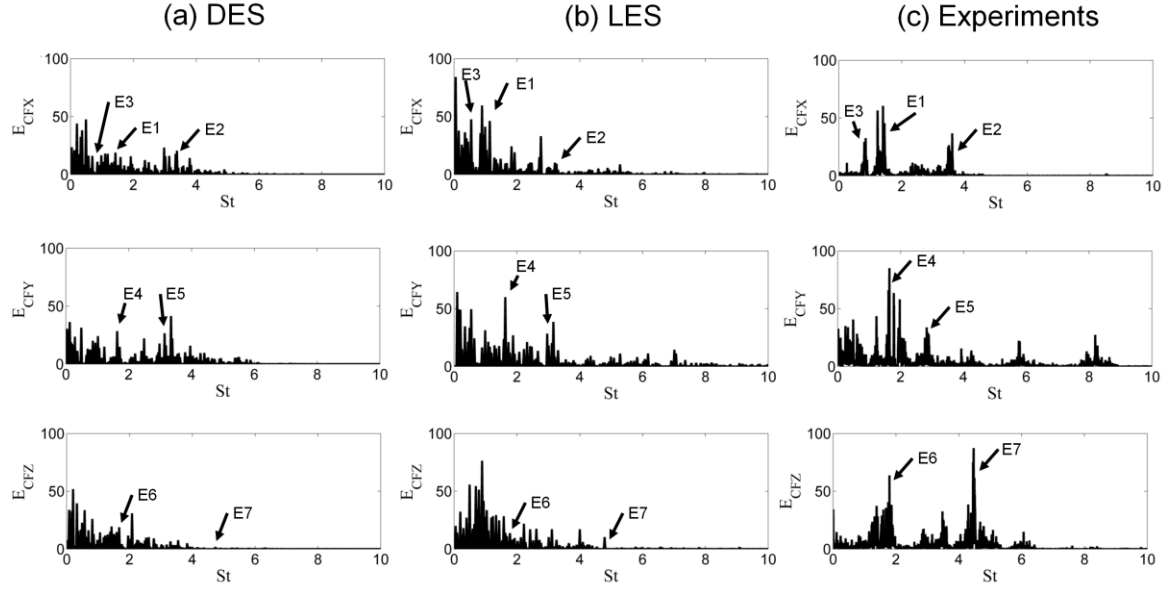


Fig. 12: Auto spectral density of the aerodynamic coefficients obtained from the fine mesh of the (a) DES simulation, (b) LES simulation, (c) experiments.

Table 4: Dominant frequencies of the auto spectrum of the force coefficients of the experimental data

| | E1 | E2 | E3 | E4 | E5 | E6 | E7 |
|----------|------|------|------|------|------|------|------|
| St | 1.40 | 3.61 | 0.85 | 1.64 | 2.83 | 1.80 | 4.47 |
| f (Hz) | 9.2 | 23.6 | 5.6 | 10.7 | 18.5 | 11.7 | 29.1 |

7 CONCLUSIONS

This is the first CFD study investigating the effect of crosswinds on a bicycle and cyclist for a range of yaw angles from 0 to 90°. RANS analysis has been performed for all yaw angles whilst DES and LES have been restricted to 15° yaw angle. A reasonably good agreement has been found between the CFD results and the experimental data across a wide range of yaw angles (average drag coefficient error of approximately 10%). The results showed that crosswinds have a significant effect on the aerodynamic force coefficients. All numerical simulations undertaken have been shown to under-predict the drag and side forces at 15° yaw angle. The LES simulations

showed the best performance of all the approaches investigated (drag coefficient error of approximately 5%). At small yaw angles, the upper body of the cyclist predominately affects the aerodynamic forces, whilst at large yaw angles the bicycle has been shown to have an increasing contribution. For the specific case of a 15° yaw angle, complex vortex structures have been identified in the flow and were found mainly in the direction of the free stream flow. These vortices predominantly appear in the flow due to the separation of the flow around the gluteus maximus, helmet, bicycle and upper body. Large vortex structures in the wake of the cyclist are predominantly found at a height of $0.6H$. The main frequencies in the time histories of the force coefficients are identified and compared with experimental data. It has been observed that both the LES and DES simulations predict all dominant frequencies found in the experimental work. It could be concluded that despite some dissimilarities between the DES and the LES results, the DES simulations is able to predict the main flow characteristics. This study shows that crosswinds significantly influence the cyclists' aerodynamic forces and the corresponding flow structures. The results therefore have significant influence with respect to the stability and safety of cyclists.

ACKNOWLEDGEMENT

All simulations have been carried out on the Birmingham Environment for Academic Research (BEAR) computational facility. This work has been funded by the University of Birmingham.

528 REFERENCES

- 529 Barry, N., Burton, D., Crouch, T., et al. (2012). Effect of crosswinds and wheel selection on the
530 aerodynamic behavior of a cyclist. *Procedia Engineering*, 34(0), 20-25. doi:
531 10.1016/j.proeng.2012.04.005
- 532 Bike Rider Blown Over By Heavy Wind. (2011, Jun 17). *7 News The Denver Channel*. Retrieved
533 from <http://www.thedenverchannel.com/news/bike-rider-blown-over-by-heavy-wind>
- 534 Bobridge blown off his bike. (2012, 11 Jan 2012). *ABC News*. Retrieved from
535 <http://www.abc.net.au/news/2012-01-11/bobridge-blown-off-his-bike/3767346>
- 536 Celik, I. B., Ghia, U., Roache, P. J., et al. (2008). Procedure for estimation and reporting of
537 uncertainty due to discretization in CFD applications. *Journal of Fluids Engineering-*
538 *Transactions of the Asme*, 130(7). doi: 10.1115/1.2960953
- 539 Cyclist's death was an accident. (2001, Nov 02). *The Guardian*. Retrieved from
540 <http://www.retfordtoday.co.uk/news/local/cyclist-s-death-was-an-accident-1-847051>
- 541 Dabnichki, P., and Avital, E. (2006). Influence of the position of crew members on aerodynamics
542 performance of two-man bobsleigh. *Journal of Biomechanics*, 39(15), 2733-2742. doi:
543 10.1016/j.jbiomech.2005.10.011
- 544 Defraeye, T., Blocken, B., Koninckx, E., et al. (2010a). Aerodynamic study of different cyclist
545 positions: CFD analysis and full-scale wind-tunnel tests. *Journal of Biomechanics*, 43(7),
546 1262-1268. doi: 10.1016/j.jbiomech.2010.01.025
- 547 Defraeye, T., Blocken, B., Koninckx, E., et al. (2010b). Computational fluid dynamics analysis of
548 cyclist aerodynamics: Performance of different turbulence-modelling and boundary-layer
549 modelling approaches. *Journal of Biomechanics*, 43(12), 2281-2287. doi:
550 10.1016/j.jbiomech.2010.04.038
- 551 Diedrichs, B. (2010). Aerodynamic crosswind stability of a regional train model. *Proceedings of*
552 *the Institution of Mechanical Engineers Part F-Journal of Rail and Rapid Transit*,
553 224(F6), 580-591. doi: Doi 10.1243/09544097jrrt346
- 554 Fintelman, D. M., Sterling, M., Hemida, H., et al. (2014). The effect of crosswind on cyclists: an
555 experimental study. *Procedia Engineering*, 72, 720-725. doi:
556 10.1016/j.proeng.2014.06.122
- 557 Flynn, D., Hemida, H., Soper, D., et al. (2014). Detached-eddy simulation of the slipstream of an
558 operational freight train. *Journal of Wind Engineering and Industrial Aerodynamics*,
559 132(0), 1-12. doi: 10.1016/j.jweia.2014.06.016
- 560 François, D., Delnero, J., Colman, J., et al. (2009). *Experimental determination of Stationary*
561 *Aerodynamics loads on a double deck Bus*. Paper presented at the 11th Americas
562 Conference on Wind Engineering, San Juan, Puerto Rico.
- 563 Godo, M. N., Corson, D., and Legensky, S. M. (2009, 5 - 8 January). An Aerodynamic Study of
564 Bicycle Wheel Performance using CFD. *47th AIAA Aerospace Sciences Meeting*
565 *Including The New Horizons Forum and Aerospace Exposition*.
- 566 Griffith, M., Crouch, T., Thompson, M., et al. (2012). *Elite Cycling Aerodynamics: Wind Tunnel*
567 *Experiments and CFD*. Paper presented at the 18th Australasian Fluid Mechanics
568 Conference, Launceston, Australia.
- 569 Griffith, M., Crouch, T., Thompson, M., et al. (2014). Computational Fluid Dynamics Study of
570 the Effect of Leg Position on Cyclist Aerodynamic Drag. *Journal of Fluids Engineering*.
- 571 Guzik, D., Harder, P., Suzuki, M., et al. (2013). 2014 Speed concept: Trek Bicycle Corporation.

572 Hanna, R. K. (2002). Can CFD make a performance difference in sport? In S. Ujihashi and S. J.
573 Haake (Eds.), *The engineering of sport 4* (pp. 17-30). Oxford: Blackwell Science Ltd.

574 Hemida, H., and Baker, C. (2010). Large-eddy simulation of the flow around a freight wagon
575 subjected to a crosswind. *Computers & Fluids*, 39(10), 1944-1956. doi:
576 10.1016/j.compfluid.2010.06.026

577 Hemida, H., and Krajnovic, S. (2010). LES study of the influence of the nose shape and yaw
578 angles on flow structures around trains. *Journal of Wind Engineering and Industrial*
579 *Aerodynamics*, 98(1), 34-46. doi: 10.1016/j.jweia.2009.08.012

580 Hemida, H., and Krajnović, S. (2009a). Exploring Flow Structures Around a Simplified ICE2
581 Train Subjected to A 30° Side Wind Using LES. *Engineering Applications of*
582 *Computational Fluid Mechanics*, 3(1), 28-41. doi: 10.1080/19942060.2009.11015252

583 Hemida, H., and Krajnović, S. (2009b). Transient Simulation of the Aerodynamic Response of a
584 Double-Deck Bus in Gusty Winds. *Journal of Fluids Engineering-Transactions of the*
585 *Asme*, 131(3). doi: 10.1115/1.3054288

586 Karabelas, S. J., and Markatos, N. C. (2012). Aerodynamics of Fixed and Rotating Spoked
587 Cycling Wheels. *Journal of Fluids Engineering-Transactions of the Asme*, 134(1). doi:
588 10.1115/1.4005691

589 Lukes, R. A., Chin, S. B., Hart, J. H., et al. (2004). The aerodynamics of mountain bicycles: the
590 role of computational fluid dynamics. In M. Hubbard, R. D. Mehta and J. M. Pallis (Eds.),
591 *The engineering of sport 5* (pp. 104-110).

592 Makowski, F. T., and Kim, S.-E. (2000). Advances in External-Aero Simulation of Ground
593 Vehicles Using the Steady RANS Equations. *SAE Technical Paper*, 2000-01-0484. doi:
594 10.4271/2000-01-0484

595 Meile, W., Reisenberger, E., Mayer, M., et al. (2006). Aerodynamics of ski jumping: experiments
596 and CFD simulations. *Experiments in Fluids*, 41(6), 949-964. doi: 10.1007/s00348-006-
597 0213-y

598 Ryan, A., and Dominy, R. G. (1998). The Aerodynamic Forces Induced on a Passenger Vehicle in
599 Response to a Transient Cross-Wind Gust at a Relative Incidence of 30°. *SAE Technical*
600 *Paper*, 980392. doi: 10.4271/980392

601 Schepers, P., and Wolt, K. (2012). Single-bicycle crash types and characteristics. *Cycling*
602 *Research International*, 2, 119-135.

603 Silva, A. J., Rouboa, A., Moreira, A., et al. (2008). Analysis of drafting effects in swimming using
604 computational fluid dynamics. *Journal of sports sciences and Medicine*, 7, 60-66.

605 Spalart, P. R., and Allmaras, S. R. (1994). A One-Equation Turbulence Model for Aerodynamic
606 Flows. *Recherche Aerospatiale*(1), 5-21.

607 Sujudi, D., and Haimes, R. (1995). Identification of swirling flow in 3-D vector fields *12th*
608 *Computational Fluid Dynamics Conference: American Institute of Aeronautics and*
609 *Astronautics*.

610 Tsubokura, M., Nakashima, T., Kitayama, M., et al. (2010). Large eddy simulation on the
611 unsteady aerodynamic response of a road vehicle in transient crosswinds. *International*
612 *Journal of Heat and Fluid Flow*, 31(6), 1075-1086. doi:
613 10.1016/j.ijheatfluidflow.2010.05.008

614 Zäidi, H., Taiar, R., Fohanno, S., et al. (2008). Analysis of the effect of swimmer's head position
615 on swimming performance using computational fluid dynamics. *Journal of Biomechanics*,
616 41(6), 1350-1358. doi: 10.1016/j.jbiomech.2008.02.005

617 Zhang, D. Y., Zheng, W. T., Ma, Q. Z., et al. (2009). Numerical Simulation of Viscous Flow
618 around Rowing Based on FLUENT. *2009 Isecs International Colloquium on Computing,*
619 *Communication, Control, and Management, Vol I*, 429-433.
620